EyeDAR: A Low-Power mmWave Tag that Senses and Communicates 3D Point Clouds to Enhance Radar Perception

Kun Woo Cho
Rice University
Houston, USA

Yaxiong Xie
University at Buffalo, SUNY
Buffalo, USA

Ashutosh Sabharwal
Rice University
Houston, USA

Abstract

Autonomous vehicles rely heavily on vision-based sensors that struggle in poor visibility in harsh weather and beyond line-of-sight. While mmWave radars work reliably in these conditions, they suffer from extremely sparse point clouds due to mirror-like reflection where most signals bounce away rather than returning to the radar. We present EyeDAR, a low-power mmWave tag deployed as roadside infrastructure that captures these lost reflections. The tag extracts arrival directions and sends these data back to the radar, providing additional point clouds to enhance radar perception. Like the human eye that uses a lens to map light angles onto different photoreceptors, EyeDAR uses a Luneburg lens to optically map arrival angles to different antennas, replacing $O(N^3)$ direction-finding algorithms with $O(N)$ detection. Combined with backscatter communication, the system operates at low power without power-hungry RF components. Our early prototype achieves 5.4° effective angular resolution with >15 dB passive gain at $7 fabrication cost. We experimentally demonstrate direction-of-arrival estimation error of $-0.2° \pm 1.8°$ with commercial 24 GHz radar.

CCS Concepts

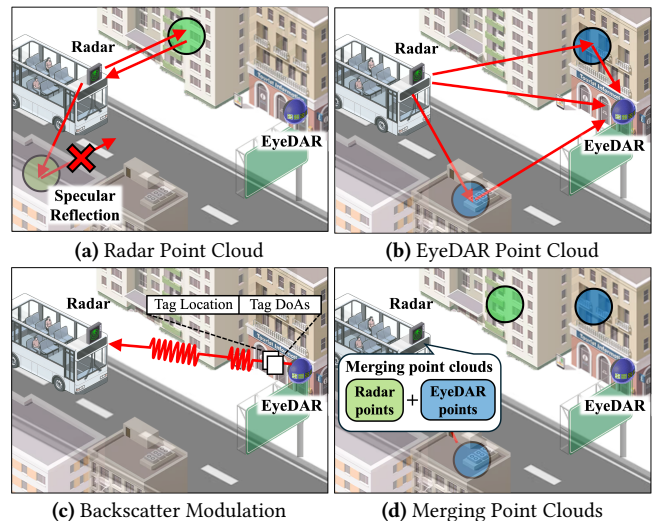• **Hardware** → **Wireless devices**; • **Networks** → **Cyber-physical networks**.

Keywords

Metamaterial, radar systems, backscatter communications, integrated sensing and communications

1 Introduction

Recent deployments of autonomous vehicles have faced critical failures in severe weather, including Tesla's Autopilot crashes in fog [22] and Waymo's navigation failures during heavy rain [18]. Currently, autonomous vehicles depend heavily on visual sensors, including cameras and LiDAR, to reconstruct 3D maps of surroundings while simultaneously locating their position. However,

Figure 1: System Overview: (a) vehicle radar suffers from sparse point clouds because most signals bounce away rather than returning; (b) EyeDARs capture some of the missed reflections from different angles; (c) EyeDARs backscatter their point cloud measurements to the vehicle using on-off keying modulation, thereby, illuminating objects invisible to the vehicle radar; (d) radar merges distributed point clouds for dense, accurate 3D perception.

these sensors are inherently vulnerable to obstructions and adverse weather conditions, causing deviations in vehicle localization and inconsistencies in mapping [5].

Radar systems operate reliably in all weather conditions along with the ability to see through obstacles and to detect in long-range. Among radar technologies, millimeter-wave (mmWave) radar systems offer significant advantages over lower frequency radars, including finer distance discrimination due to their large bandwidth (up to 4 GHz in the 77-81 GHz automotive band) and improved angular resolution from smaller antenna dimensions. However, mmWave radars create point clouds two orders of magnitude sparser than LiDARs [19]. At mmWave, signals exhibit specular reflection, behaving like light bouncing off mirrors rather than diffused scattering in the visible light spectrum. Consequently, most reflected signals do not return to the radar, leaving vast area invisible. Also, ghost points due to multiple signal bounces, sidelobes from strong reflectors, and ground clutters create false detections that pollute the sparse point cloud [16, 19]. Combined with their narrow field-of-view, current radar systems cannot serve as primary perception sensors.

In this work, we introduce EyeDAR, a low-power mmWave tag deployed as roadside infrastructure to enhance automotive radar perception. As illustrated in Fig. 1, EyeDARs capture reflection
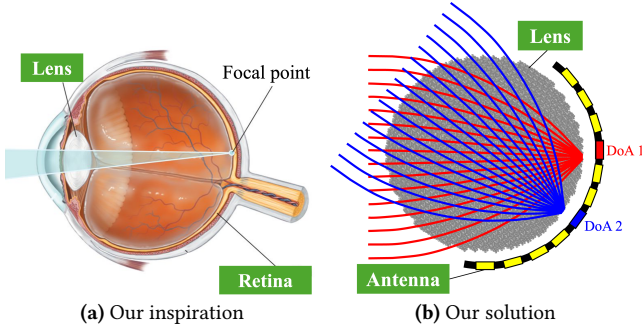
Figure 2: Lens-based direction finding with O(N) complexity. Like human eyes where the lens focuses light onto photoreceptors, EyeDAR consists of (1) a Luneburg lens to focus signals from any direction and (2) miniaturized antennas to detect the focal point and determine direction-of-arrival.

Table 1: Comparison to existing mmWave backscatter systems.

Works	Design	Local. & Ident.	Comm.	Env. Sensing
MilliMetro [24]	VAA	✓	✗	✗
BiScatter [17]	VAA	✓	✓	✗
Milback [15]	LWA	✓	✓	✗
UniScatter [20]	Luneburg	✓	✓	✗
EyeDAR	Luneburg	✓	✓	✓

signals that would otherwise bounce away due to specular reflection and send their point cloud measurements back to the radar to increase point cloud density. Also, EyeDAR point clouds could serve as spatial anchors to filter ghost points. Our work addresses three design challenges for practical deployment: (1) high-gain architecture to capture weak non-line-of-sight (NLoS) reflections and extend communication range, (2) milliwatt-level power consumption through novel optics-based direction-finding and backscatter communication, and (3) cost-effective fabrication using standard PCB and 3D printing. Our key innovation lies in joint sensing and communication: each tag extracts direction-of-arrivals (DoAs) from reflected radar signals, then encodes this data via backscatter modulation that eliminates need for power-hungry RF components.

(1) Human-eye inspired optical direction finding. Direction finding is expensive both computationally and in power consumption. Current radars use linear antenna arrays that measure phase difference across antennas to determine DoAs. However, angular resolution directly scales with array size and power. Commodity mmWave radars typically achieve only 15-30° resolution, [11, 12], while reaching <2° requires 20 W power and bulky form factors [13]. Processing also requires computationally intensive algorithm like the multiple signal classification (MUSIC) with $O(N^3)$ complexity [21]. We overcome these limitations using passive optics inspired by human eyes. As illustrated in Fig. 2, EyeDAR uses a Luneburg lens whose gradient refractive index focuses incident radar signals to angle-dependent, focal points on its opposite surface. This is similar to human eye's lens that focuses light from different angles onto specific locations on the retina. Antennas surrounding the Luneburg lens detect these focal points through simple power measurement, reducing $O(N^3)$ processing to $O(N)$ threshold detection. Our design breaks the trade-off: angular resolution now depends on antenna spacing rather than array size. Also, the lens provides >15 dB passive gain through beam focusing, eliminating the need for amplifiers. With current patch antennas, we achieve 5.4° effective resolution, with potential for sub-2° using denser metamaterial antennas.

(2) Integrated backscatter sensing and communication. Backscattering enables ultra-low power communication by modulating and

reflecting existing signals back to the source rather than generating new signals. Prior mmWave backscatter tags use retroreflectors so that vehicles can locate and receive transportation updates from the tags [15, 17, 20, 24]. In contrast, EyeDAR tags *sense surrounding objects* and communicate these observations to vehicle via backscattering. Our architecture seamlessly integrate sensing and communication through two modules: the front-end has a Luneburg lens and antennas that capture spatial information, while the back-end uses an RF switch, power detector, and microcontroller (MCU) to process and communicate this data. The tag alternates two modes. During sensing, the switch sequentially connects each antenna with the power detector to measure signal strength and identify DoAs. During communication, the MCU encodes tag ID, location, and detected DoAs using on-off keying (OOK) where bit '0' absorbs radar signals by connecting antennas to RF detector and bit '1' retro-reflects them by grounding antennas. This backscatter communication allows uninterrupted radar operation while simultaneously delivering EyeDAR point cloud data.

We build early prototype hardware of EyeDAR using in-lab 3D printing and PCB fabrication. We test our prototype with a commercial 24 GHz automotive radar to demonstrate accurate DoA estimation (-0.2° ± 1.8° error) and reliable backscatter communication. We propose a resonant metamaterial antenna to reduce antenna spacing from $\lambda/2$ to $\lambda/6$, enabling 3× denser arrays for sub-2° resolution and wideband operation.

2 Background and Related Works

This section provides background on mmWave backscatter communication and metamaterials.

2.1 Backscatter Communication

Backscatter enables ultra-low power communication (tens of µW) by modulating existing signals (*e.g.,* switching between reflecting them back and absorbing them), rather than generating new signals. MilliMetro [24] proposes long-range tag localization using Van Atta antenna (VAA) arrays, allowing vehicles to identify road signs in fog, but only transmits tag ID. BiScatter [17] and MilBack [15] add downlink capability for bi-directional communication between the radar and tags. However, these retroreflector antennas often suffer from low gain, narrow bandwidth, and limited angular coverage. While UniScatter [20] uses a Luneburg lens to provide high gain, ultra-wide bandwidth, and full 3D angular coverage, it still uses tags as simple reflectors for tag localization and roadside signage. EyeDAR is the first to use tags as environmental sensors, extracting and communicating DoA information to provide dense 3D point clouds for radar perception.

2.2 Metamaterials

Metamaterials are artificially-engineered structures that provide electromagnetic properties that do not exist in natural material. We categorize them into two classes: resonant metamaterials and gradient index (GRIN) metamaterials.

Resonant metamaterials. They consist of periodic arrays of sub-wavelength elements (typically $\lambda/6$ or less) that interacts with EM waves through local resonances. Each element commonly resembles split-ring resonators (SRR) and/or complementary LC resonators (CSRR), fabricated as copper patterns on planar PCB substrates. Loading these structures with active components, such as varactors or PIN diodes, make them reconfigurable. Recent works demonstrate resonant metamaterials that alter existing signals in the environment with precise control over phase, amplitude, polarization, and propagation direction [6–8, 14, 23, 26]. While they provide strong wave manipulation, resonant metamaterials often suffer from narrow bandwidth.
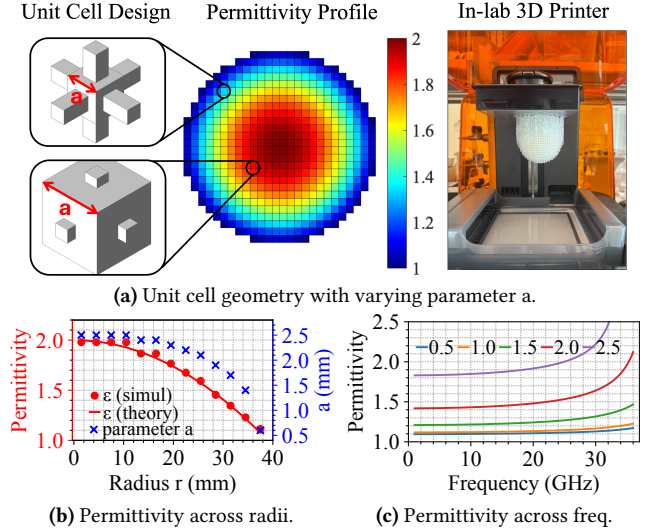
Gradient-Index (GRIN) metamaterials. Gradient index (GRIN) metamaterials manipulate waves through spatially varying refractive index rather than resonances. A key example is the Luneburg lens, a spherical structure where the refractive index gradually decrease from 2 (center) to 1 (surface). As waves propagate through the lens, this gradient continuously bends waves until they converge at a focal point on the opposite side. Unlike resonant metamaterials, they are fully passive and operate omni-directionally (identical response from any angle) with extremely wide bandwidth and high focusing gain. Luneburg lenses are currently used in various applications. Military aircraft like the F-22 and F-35 use them as radar reflectors to control visibility [10], and automotive radar companies use them as a radar to expand field-of-view and range [28]. Bahr et al. [3] used them as retroreflectors to create a radio-frequency equivalent to optical motion capture systems like Vicon. UniScatter [20] recently used them for wideband mmWave retroreflection in backscatter communication. However, all existing applications treat the lens simply as a reflector or beam director. EyeDAR exploits the Luneburg lens's focusing property as a passive computational element, transforming incident angles into detectable focal positions. This allows our tag to extract and communicate DoA information without $O(N^3)$ signal processing.

3 EyeDAR System Design

Figure 1 illustrates the system overview of EyeDAR. Our design consists of two integrated modules: a human-eye-inspired sensor that extracts DoA information from incident radar signals, and a backscatter communication module that encodes and transmits this spatial data back to the radar.

3.1 Human Eye-Inspired Sensor Design

To design the most efficient direction-finding system, we draw inspiration from the human eye, which achieves 290 µm resolution at 1 meter [4] across a 150° field-of-view [9] while processing 400-790 THz bandwidth [27]. The key principle is simple: a lens focuses incoming light from different angles onto specific location on the retina, where photoreceptors detect the spatial pattern. We apply this using a Luneburg lens to focus radar signals and surrounding

(a) Unit cell geometry with varying parameter a.

(b) Permittivity across radii. **(c)** Permittivity across freq.

Figure 3: Luneburg lens design and characterization. (a) unit cell design with different cube dimension a that controls permittivity; (b) permittivity across radial distance: theoretical (red line) vs. simulated values (red dots) with corresponding a values (blue markers); (c) permittivity across frequency for different a values (0.5-2.5 mm).
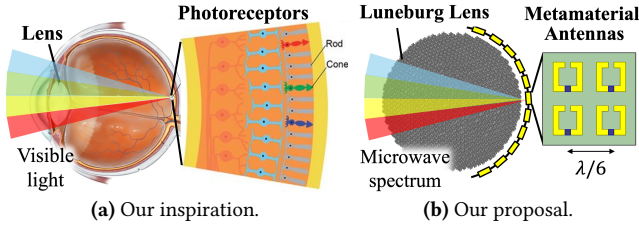
antennas to detect focal positions. This approach replaces computationally intensive algorithm with $O(N^3)$ complexity [21] with simple power detection in $O(N)$.

Luneburg Lens Design. The Luneburg lens is a spherical gradient-index structure where the refractive index n varies radially according to $n = \sqrt{\epsilon} = \sqrt{2 - (r/R)^2}$, where ϵ is the permittivity, R is the lens radius, and r is the distance from any point to the sphere center. The permittivity profile of the Luneburg lens is shown in Fig. 3a. This profile causes incident plane waves from any direction to converge at a focal point on the opposite hemisphere.

Instead of layering multiple materials with different permitivities to create the gradient, we discretize the lens into unit cells of a single material and vary each cell's geometry to achieve the desired permittivity profile. As shown in Fig. 3a, each unit cell consists of six fixed rods with a variable central cube (size a) that controls permittivity. Specifically, increasing the cube size a increases the permittivity. Fig. 3b validates our design accuracy as simulated permittivity of our unit cells (red dots) closely match the theoretical profile (red line), with corresponding a values indicated by blue markers. Fig. 3c shows the permittivity remains stable across frequencies up to 32 GHz for various a values (0.5-2.5 mm). We fabricated a 40 mm radius lens using our in-lab 3D printer with resin that costs approximately $7.

Antenna Design. Like how photoreceptor spacing determines the angular resolution of the human eye, antenna spacing around the Luneburg lens dictates our angular resolution. Currently, we surround the half of lens with patch antennas with $\lambda/2$ spacing. To improve resolution beyond the physical spacing, we implement a simple centroid-based interpolation. We first select only antennas with signal power above a threshold, then take the three strongest

(a) Our inspiration.　　**(b)** Our proposal.

Figure 4: Design consideration. (a) the human eye achieves wide bandwidth and high resolution through densely packed cone photoreceptors, each sensitive to red, green, or blue lights; (b) our metamaterial antennas with $\lambda/6$ spacing around Luneburg lens, where different antennas are tuned to specific frequencies for wideband operation.

and compute their weighted center: $x_{peak} = \sum x_i y_i / \sum y_i$, where x_i is antenna position and y_i is signal strength. This allows sub-antenna resolution when the focal point falls between elements.
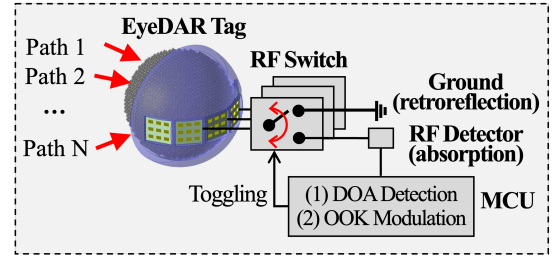
Current antenna design faces limitations in large spacing and narrow bandwidth. Fig. 4 illustrates our proposed solution. Resonant metamaterial antennas (*e.g.*, SRR) reduce element spacing from $\lambda/2$ to $\lambda/6$, fitting 3× more antennas in the same area. Each metamaterial antenna consists of a metallic ring with a gap that forms an LC resonant circuit, and we can load varactor diodes on this design for dynamic phase control. By adjusting phases to create constructive interference at the radar receiver, our tag can extend communication range beyond conventional backscatter limits.

For bandwidth enhancement, we draw inspiration from the human eye's trichromatic vision, where different cone types respond to specific wavelengths (blue, green, red). Similarly, we propose interleaving metamaterial antennas tuned to different center frequencies, creating a wideband array that matches the Luneburg lens's wide frequency response.
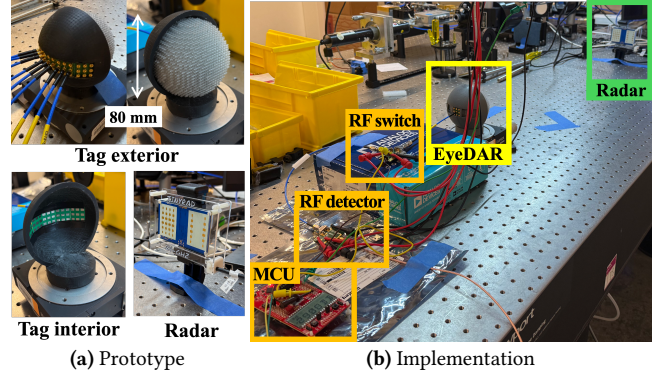
3.2 Backscatter Communication Design.

The communication module encodes detected DoA information for transmission back to the radar. As shown in Fig. 5, this module contains three key components: RF switch network, power detector, and microcontroller (MCU).

The system alternates between sensing and communication modes through RF switches. The MCU sends control signals through its DAC output pins to operate these switches, connecting each antenna to either the power detector (sensing) or ground (backscattering). In sensing mode, the MCU cycles through all antennas, connecting each one to the power detector in sequence. The detector measures how much signal each antenna receives, and the MCU reads these measurements through its ADC input pins and determines DoAs. For communication, the MCU encodes tag ID, tag location, and detected DoAs using on-off keying (OOK). To send a '1' bit (on state), the switch connects the antenna to ground, creating a strong reflection back to the radar. To send a '0' bit (off state), the switch connects the antenna to the power detector, which has 50Ω impedance matching, absorbing the signal instead of reflecting it. This reflection-absorption pattern creates a 15 dB difference, which is sufficient for reliable detection at the radar.

Figure 5: Backscatter Architecture

(a) Prototype　　**(b)** Implementation

Figure 6: EyeDAR prototype hardware and implementation.

Owing to Luneburg lens's omni-directional focusing, EyeDAR can handle signals from multiple paths simultaneously. Signals from different angles focus at distinct points on the lens surface, where corresponding antennas independently retro-reflect each beam to its source. This provides both path redundancy and significant gain for weak NLoS signals. The lens contributes >15 dB gain in each direction, yielding >30 dB round-trip gain without power-hungry components.
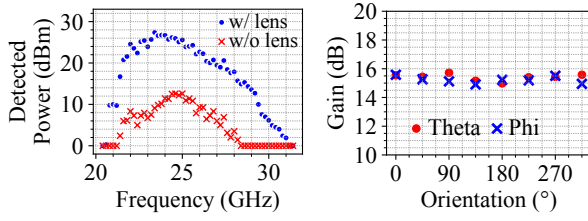
While this work considers a single radar scenario, our future work will explore bi-directional communication where each radar sends a unique ID in its downlink transmission, allowing tags to differentiate between multiple radar sources.
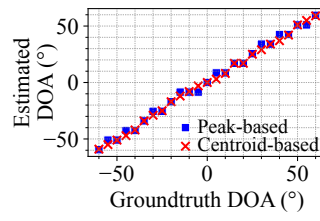
4 Implementation

This section presents our prototype hardware and experimental testbed. Fig. 6a shows our fabricated 40 mm radius Luneburg lens with integrated patch antenna array. We 3D-printed the lens using our in-lab 3D printer with resin ($\varepsilon_r = 2.65$). Our custom enclosure holds the antenna array covering the half of hemisphere. There are 45 patch antennas, arranged in 3 rows × 15 columns, uniformly spaced at 8.5° intervals. They are fabricated on Rogers substrate, providing 120° field-of-view. We validated the antenna design using ANSYS HFSS. The prototype uses Analog Devices ADRF5020 RF switches [2] operating up to 30 GHz to route signals between sensing and backscattering modes. The switch connects an antenna to either a power detector [1] or ground. The Texas Instruments MSP430FR6989 microcontroller [25] controls the system with 125 *ns* switching speed.

We evaluate EyeDAR using an Analog Devices TinyRad FMCW radar [11] operating at 24 GHz with 250 MHz bandwidth. The radar
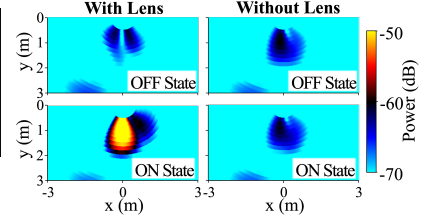
Figure 7: Microbenchmark. The gain of Luneburg Lens across different frequencies (left) and orientations in azimuth and elevation (right).

Figure 8: DOA estimation accuracy with peak-based and centroid-based method.

Figure 9: Radar measurement of off (absorption) and on state (retro-reflection with and without the lens.

features two transmit and four receive antenna arrays. For wideband characterization, our microbenchmark uses a signal generator producing from 10 to 20 GHz signals, followed by a frequency doubler to reach from 20 to 40 GHz. The doubled signals are transmitted through a WR-28 horn antenna. For all measurements, we place the transmitter 17 inches from the EyeDAR prototype.

5 Evaluation

In this section, we first present microbenchmark results characterizing the Luneburg lens performance. We then demonstrate EyeDAR's feasibility in direction finding and backscatter communication.

5.1 Microbenchmarks

We evaluate our Luneburg lens's gain across different frequencies and incident angles. All measurements are scaled such that 0 dB corresponds to the detector noise floor.
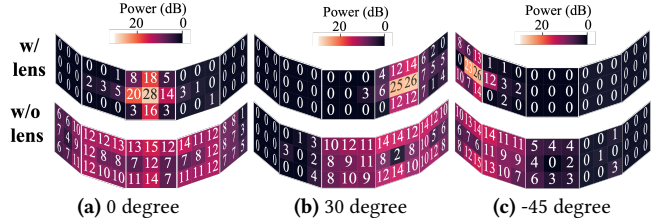
Lens Gain. Figure 7 (left) shows power measurements with and without the Luneburg lens from 20 to 32 GHz. The patch antenna alone operates from 21 to 28 GHz with peak gain at approximately 24.5 GHz. Adding the lens provides >15 dB gain improvement from 21 to 29 GHz, with maximum improvement of 18.3 dB at 23 GHz. While our simulations show lens operation to 32 GHz, measured bandwidth is limited by cables and antenna losses, not the lens.

Lens Coverage. Figure 7 (right) shows the lens's focusing gain as we rotate the lens in different azimuth (theta) and elevation (phi) angles at 24 GHz. The gain remains consistent, varying by less than 0.7 dB across all measured angles, validating the Luneburg lens's omnidirectional focusing capability.
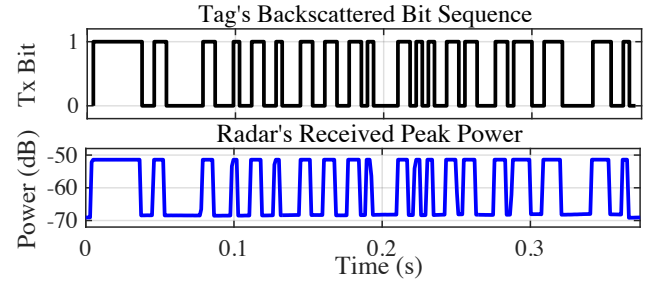
5.2 Direction-of-Arrival Estimation

Figure 8 evaluates EyeDAR's DoA estimation accuracy using our 3×15 antenna array with 8.5° spacing. We sweep the incident beam angle from -60° to +60° in 5° increments and compare two estimation methods: peak detection and centroid-based interpolation (described in Section 3). The peak-based method achieves $0.68° \pm 2.7°$ error. The centroid-based method significantly improves accuracy, achieving $-0.2° \pm 1.8°$ error, showing that simple weighted averaging can effectively interpolate between adjacent antenna positions. This 1.8° precision corresponds to an effective angular resolution of approximately 5.4° (3σ).

Figure 10 shows the power distribution across all antennas for incident beam angles of 0°, 30°, and -45°. With the lens, incident signals focus to a sharp peak spanning only 1 or 2 antennas, while without the lens, power spreads across most antennas with minimal

(a) 0 degree   **(b)** 30 degree   **(c)** -45 degree

Figure 10: Lens focusing effect on antenna array. Power distribution across antenna array for different incident beam angles (0°, 30°, -45°) with and without the lens.

Figure 11: Real-time OOK modulation. Backscattered bit sequence (top) successfully decoded by radar (bottom).

variation, making DoA estimation nearly impossible. Note that without the lens, the strongest signal often doesn't appear at the antenna directly facing the transmitter, as seen in Fig. 10b and Fig. 10c, likely due to signal interference.

5.3 Backscatter Performance

Figure 9 shows radar's digital beamforming response over range and azimuth during backscatter modulation. In the 'off' state (top), the center antenna absorbs signals through the 50Ω detector, creating a null in the beamformed response while surrounding reflections remain visible. In the 'on' state (bottom), the same antenna retroreflects strongly, producing a dominant peak in the spatial map. This clear distinction in the beamformed response demonstrates reliable OOK modulation for backscatter communication. Without the lens, no distinguishable change occurs between two states.

Figure 11 shows the tag's backscattered bit sequence (top) and the radar's decoded signal (bottom). Each bit is backscattered over a 2 ms duration, while the radar samples at 1 ms frame. For each

radar frame, we extract the maximum value from the digital beam-formed map to quantify backscatter strength. It shows detected peaks closely align the transmitted sequence, demonstrating that the tag successfully modulates bit-0 and bit-1 with 18 dB modulation depth.

6 Conclusion and future works

This paper presents EyeDAR, the first mmWave tag that performs environmental sensing for enhanced radar perception. Our prototype achieves 5.4° resolution with >15 dB passive gain, demonstrating the feasibility of infrastructure-deployed sensing tags. In future, we will explore several directions:

- We will develop tunable metamaterial antennas to achieve <2° angular resolution, wideband operation via frequency-diverse elements, and extended communication range.
- While our current system provides only angular information, complete 3D point cloud reconstruction requires range information. We will investigate range extraction techniques to estimate distances between environmental reflectors and the tag.
- We will implement lightweight algorithms that fuse measurements from multiple tags with vehicle radar data. By pre-computing geometric transformation matrices based on known tag positions, the system can merge distributed observations through simple matrix operations.

Acknowledgments

References

[1] Analog Devices Incorporated. *LTC5596*, 2016. Rev. A.

[2] Analog Devices Incorporated. *ADRF5020*, 4 2020. Rev. B.

[3] R. A. Bahr, A. O. Adeyeye, S. Van Rijs, and M. M. Tentzeris. 3d-printed omni-directional luneburg lens retroreflectors for low-cost mm-wave positioning. In *2020 IEEE International Conference on RFID (RFID)*, pages 1–7, 2020.

[4] F. Campbell and D. Green. Optical and retinal factors affecting visual resolution. *The Journal of physiology*, 181(3):576, 1965.

[5] C. Campos, R. Elvira, J. J. G. Rodríguez, J. M. M. Montiel, and J. D. Tardós. Orb-slam3: An accurate open-source library for visual, visual–inertial, and multimap slam. *IEEE Transactions on Robotics*, 37(6):1874–1890, 2021.

[6] K. Chen, Y. Feng, F. Monticone, J. Zhao, B. Zhu, T. Jiang, L. Zhang, Y. Kim, X. Ding, S. Zhang, et al. A reconfigurable active huygens' metalens. *Advanced materials*, 29(17):1606422, 2017.

[7] K. W. Cho, Y. Ghasempour, and K. Jamieson. Towards dual-band reconfigurable metasurfaces for satellite networking. In *Proceedings of the 21st ACM Workshop on Hot Topics in Networks*, HotNets '22, page 17–23, New York, NY, USA, 2022. Association for Computing Machinery.

[8] K. W. Cho, M. H. Mazaheri, J. Gummeson, O. Abari, and K. Jamieson. mmWall: A steerable, transflective metamaterial surface for NextG mmWave networks. In *20th USENIX Symposium on Networked Systems Design and Implementation (NSDI 23)*, pages 1647–1665, Boston, MA, Apr. 2023. USENIX Association.

[9] C. A. Curcio, K. R. Sloan, R. E. Kalina, and A. E. Hendrickson. Human photoreceptor topography. *Journal of comparative neurology*, 292(4):497–523, 1990.

[10] S. D'Urso and D. Cenciotti. U.s. and dutch f-35s have flown without radar reflectors during first week of 'falcon strike 2022. *The Aviationist*.

[11] A. D. Incorporated. Evaluating the tinyrad 24 ghz demonstration platform. https://www.analog.com/en/design-center/evaluation-hardware-and-software/evaluation-boards-kits/eval-tinyrad.html, 2025.

[12] T. I. Incorporated. 76-ghz to 81-ghz high-performance automotive mmic. https://www.ti.com/product/AWR1243, 2025.

[13] T. I. Incorporated. Mmwcas-rf-evm. https://www.ti.com/tool/MMWCAS-RF-EVM, 2025.

[14] M. Liu, D. A. Powell, Y. Zarate, and I. V. Shadrivov. Huygens' metadevices for parametric waves. *Physical Review X*, 8(3):031077, 2018.

[15] H. Lu, M. Mazaheri, R. Rezvani, and O. Abari. A millimeter wave backscatter network for two-way communication and localization. In *Proceedings of the ACM SIGCOMM 2023 Conference*, ACM SIGCOMM '23, page 49–61, New York, NY, USA, 2023. Association for Computing Machinery.

[16] N. Mehrotra, D. Pandey, A. Prabhakara, Y. Liu, S. Kumar, and A. Sabharwal. Hydra: Exploiting multi-bounce scattering for beyond-field-of-view mmwave radar. In *Proceedings of the 30th Annual International Conference on Mobile Computing and Networking*, ACM MobiCom '24, page 1545–1559, New York, NY, USA, 2024. Association for Computing Machinery.

[17] R. Okubo, L. Jacobs, J. Wang, S. Bowers, and E. Soltanaghai. Integrated two-way radar backscatter communication and sensing with low-power iot tags. In *Proceedings of the ACM SIGCOMM 2024 Conference*, ACM SIGCOMM '24, page 327–339, New York, NY, USA, 2024. Association for Computing Machinery.

[18] E. Pauda. Apd officers move waymo vehicles pulled over during severe weather. *Yahoo News*.

[19] A. Prabhakara, T. Jin, A. Das, G. Bhatt, L. Kumari, E. Soltanaghai, J. Bilmes, S. Kumar, and A. Rowe. High resolution point clouds from mmwave radar. In *2023 IEEE International Conference on Robotics and Automation (ICRA)*, pages 4135–4142, 2023.

[20] K. Qian, L. Yao, K. Zheng, X. Zhang, and T. N. Ng. Uniscatter: a metamaterial backscatter tag for wideband joint communication and radar sensing. In *Proceedings of the 29th Annual International Conference on Mobile Computing and Networking*, ACM MobiCom '23, New York, NY, USA, 2023. Association for Computing Machinery.

[21] M. Rubsamen and A. B. Gershman. Direction-of-arrival estimation for nonuniform sensor arrays: From manifold separation to fourier domain music methods. *IEEE Transactions on Signal Processing*, 57(2):588–599, 2009.

[22] D. Shepardson and A. Sriram. Us probes tesla's full self-driving software in 2.4 mln cars after fatal crash. *Reuters*.

[23] D. R. Smith, J. B. Pendry, and M. C. Wiltshire. Metamaterials and negative refractive index. *Science*, 305(5685):788–792, 2004.

[24] E. Soltanaghaei, A. Prabhakara, A. Balanuta, M. Anderson, J. M. Rabaey, S. Kumar, and A. Rowe. Millimetro: mmwave retro-reflective tags for accurate, long range localization. In *Proceedings of the 27th Annual International Conference on Mobile Computing and Networking*, MobiCom '21, page 69–82, New York, NY, USA, 2021. Association for Computing Machinery.

[25] Texas Instruments Incorporated. *MSP-EXP430FR6989*, 7 2015. Rev. A.

[26] Z. Wu, Y. Ra'di, and A. Grbic. Tunable metasurfaces: A polarization rotator design. *Physical Review X*, 9(1):011036, 2019.

[27] G. Wyszecki and W. S. Stiles. *Color science: concepts and methods, quantitative data and formulae*. John wiley & sons, 2000.

[28] H. Xin, M. Liang, and S. Cao. Automotive radar using 3d printed luneburg lens, May 24 2022. US Patent 11,340,342.